

Nanoscale

Accepted Manuscript



This is an *Accepted Manuscript*, which has been through the Royal Society of Chemistry peer review process and has been accepted for publication.

Accepted Manuscripts are published online shortly after acceptance, before technical editing, formatting and proof reading. Using this free service, authors can make their results available to the community, in citable form, before we publish the edited article. We will replace this *Accepted Manuscript* with the edited and formatted *Advance Article* as soon as it is available.

You can find more information about *Accepted Manuscripts* in the [Information for Authors](#).

Please note that technical editing may introduce minor changes to the text and/or graphics, which may alter content. The journal's standard [Terms & Conditions](#) and the [Ethical guidelines](#) still apply. In no event shall the Royal Society of Chemistry be held responsible for any errors or omissions in this *Accepted Manuscript* or any consequences arising from the use of any information it contains.

Cite this: DOI: 10.1039/c0xx00000x

www.rsc.org/xxxxxx

ARTICLE TYPE

Three-dimensional scanning near field optical microscope (3D-SNOM) imaging of random arrays of copper nanoparticles: implications for plasmonic solar cell enhancement

Sabastine Ezugwu,^a Hanyang Ye^a and Giovanni Fanchini^{*,a,b}⁵ Received (in XXX, XXX) Xth XXXXXXXXX 20XX, Accepted Xth XXXXXXXXX 20XX

DOI: 10.1039/b000000x

In order to investigate the suitability of random arrays of nanoparticles for plasmonic enhancement in the visible-near infrared range, we introduced three-dimensional scanning near-field optical microscopy (3D-SNOM) imaging as an efficient technique to probe the amount of near-field radiation scattered by random systems of nanoparticles at heights from zero to several hundred nm from their surface. We demonstrated our technique using random arrays of copper nanoparticles (Cu-NPs) as a function of the particle diameter and concentration. Bright regions in the 3D-SNOM images, corresponding to constructive interference of forward-scattered plasmonic waves, were obtained at heights $\Delta z \geq 220$ nm from the surface for random arrays of Cu-NPs of ~60-100 nm in diameter. These heights are too large to use Cu-NPs for light harvesting in thin film solar cells, which are typically no thicker than 200 nm. Using a 200-nm transparent spacer between the system of Cu-NPs and the solar cell active layer, we demonstrate that forward-scattered light can be conveyed in a 200 nm thin film solar cells. This architecture increases the solar cell photoconversion efficiency by a factor 3. Our 3D-SNOM technique is general enough for being suitable to a large number of other applications in nanoplasmonics.

20

1. Introduction

Plasmon resonance can increase the optical response of thin film solar cells and other optoelectronic devices in spectral regions in which semiconductors are poorly absorbing. The essential properties of metallic nanoparticles that are required for such application are field amplification and strong light scattering associated with the excitation at their plasmon frequencies.¹⁻³ Very strong plasmonic field enhancements may be achieved if they are generated in the proximity of small metallic particles of appropriate shape and size and may be of near-field in nature.^{4, 5} When nanoparticles scatter light in a solar cell, this effect may result in strong absorption of light inside the photoactive region and the generation of electron-hole pairs in the device is subsequently enhanced. For solar cells and other optoelectronic devices to take advantage of the beneficial effects of these enhancements, it is essential to correlate the intensity of the scattered electric field, described in terms of a series of electrical multipoles⁶⁻⁸ with the size⁹, and concentration¹⁰ of the metallic nanoparticles, as well as their position in relation to the photoactive semiconducting layer of the device.¹¹

In relation of the dielectric function of a metal, it is shown that the electric field localized in the proximity of metallic nanoparticles induces charge polarization of free electrons,

yielding to their coherent excitation.⁵ In the far field, such coherent oscillations are highly screened as long as their frequency is below the plasmon frequency and the metal is highly reflective.¹² The plasmon frequency thus provides the framework for describing the effectiveness of a plasmonic enhancement layer. Due to its relatively low plasmon frequency, copper has been considered for plasmonic photovoltaic applications at infrared frequencies, for which it is highly reflective in the far field, but seldom for visible light, because it exhibits strong optical absorption and poor reflectivity in the far field in that range.¹³ However, strong Mie scattering and forward-scattering in the near field at frequencies above the plasmon resonance of metallic nanoparticles can also be useful to enhance light collection in thin film devices, if appropriately conveyed in their active region.⁶ Plasmon resonance effects have equally triggered considerable research interest with applications in other areas. For instance, an increase in electroluminescence of about 12-orders of magnitude in light emitting diode (LED) has been reported^{14,15}, in which metal nanoparticles were used to increase the external quantum efficiency from thin silicon-on-insulator LED. More recently, it has been shown that magneto-optical effects can be remarkably increased if implemented with nanostructured plasmonic crystals¹⁶⁻¹⁸. In the later reports, multilayered films covered by silver-capped nanospheres

enhanced light transmission in the film due to enhanced interaction of light with surface plasmons. However, for these and other applications, copper is preferable over other metals commonly used for plasmonic enhancement in the visible, including silver and gold, because of its cost-effectiveness.

In the specific case of copper,¹⁹ that can be easily oxidized,^{20,21} it is extremely important to grow the nanoparticles by physical deposition techniques that present significant advantages over wet chemistry methods that predispose the fabricated NPs to

contamination and oxidation by the precursor residual materials, their by-products and the immediate environment. In physical deposition techniques, particle growth takes place in ultra-high vacuum (UHV), thereby minimizing the problems of contamination and oxidation. These techniques, including sputtering, thermal and ion-beam evaporation and pulsed laser deposition can be used to deposit a variety of thin films and nanoparticles and are easily adaptable for large scale and industrial processes.²⁴

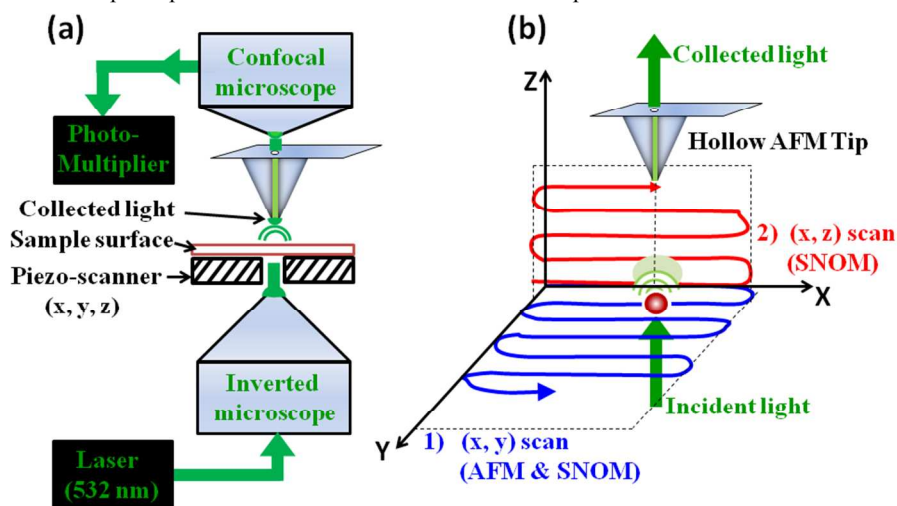


Fig. 1 (a) Schematic of collection mode operation of the Witec Alpha 300S system we used for 3D-SNOM study of Cu-NPs. The piezo-scanner can be manipulated to move in any of the three x , y , z directions. (b) Schematic diagram of the 3D SNOM configuration for measurements of topography and light scattering from Cu-NPs. Collection-mode and topography images are simultaneously obtained from an (x, y) AFM/SNOM scan at $z = 0$ while an (x, z) SNOM cross section scan at $y = \text{const.}$ is used to obtain the position of light scattered by the nanoparticles at different heights from the sample surface.

In order to explore the suitability of Cu-NPs grown by direct-current biased, radio-frequency (RF) magnetron sputtering for plasmonic applications in thin film solar cells, we are here introducing three-dimensional (3D) scanning near-field optical microscopy (3D-SNOM) at 532 nm wavelength as a useful tool to directly image the amount of light that is forward-scattered in the near field from layers of metallic nanoparticles. This wavelength has been specifically chosen because it is situated in the proximity of the maximum of the AM 1.5 solar spectrum that is customarily used to design photovoltaics and other solar devices.²³ SNOM is a nano-optical imaging technique that enables light-matter interaction for the purpose of extracting relevant information about nanoscale objects.²⁴ Aperture-type SNOM involves electromagnetic interaction of two distinct nano-objects for which the principle of linear superposition can be invoked: a ‘probe’ nano-hole and a ‘sample’ nano-object (that in our case will be a Cu-NP in our sample). In the past, ‘nano-hole’ probes were typically tapered optical fibres. In our state-of-the-art equipment, the nano-hole is a nanometric aperture machined at the end of an atomic force microscope cantilever. The 3D-SNOM method that we have developed for the present study is depicted in panel (a) of Figure 1. With this method, the sample is illuminated from the 532-nm laser using an inverted microscope underneath the sample and an aperture-type SNOM probe attached to an atomic force microscope is utilized to collect light in the near field at variable distances z over the sample surface, controlled using a piezoelectric scanner, while maintaining the usual raster scan of the optical probe constant along the x - or y -axis (see panel b). At each point (x, y, z) the amount of light

collected from the aperture of the SNOM probe is proportional to the light forward-scattered by the sample and is received by an upright confocal optical microscope focused on the tip hole and the intensity is measured using a photomultiplier. This configuration allows us to map the forward-scattered waves of the electric field arising from Mie scattering from various centers in our random arrays of Cu-NPs situated at the sample surface. The usefulness of our method for designing Cu-NP layers for plasmonic photovoltaic applications will be demonstrated.

2. Results and Discussion

2.1 - Samples used in this study

A distinct advantage of our method for growing Cu-NPs is that the direct-current biased, RF magnetron sputtering system in which our random arrays of Cu-NPs have been deposited and annealed (see Experimental section for details) is directly attached to an inert-atmosphere glove box in which the samples can be analyzed and encapsulated for minimal oxygen exposure. Organic solar cell fabrication has also been carried on in the same glove box, which is equipped with a built-in spin coater and an AM 1.5 solar simulator for device testing. The aperture-type scanning near-field optical microscope used for 3D-SNOM characterization is also located inside a sealed enclosure that can be filled with inert gas, and in which samples can be transferred from the glove box in sealed bags. In order to demonstrate the importance of minimizing oxygen contamination of our Cu-NP samples, we investigated the degree of oxidation of Cu-NPs when annealed in air as well as in our nitrogen-filled glove box. The

energy dispersive x-ray (EDX) spectra of two Cu-NP samples, annealed at 300°C in air and in glove box, as well as reference as-deposited sample are displayed in Figure 2, panels a, b and c, respectively. This sample was sputtered on Si substrate for 3 minutes at 75W RF power, 0V dc bias and 9 Pa Ar pressure and divided in two parts that were annealed separately.

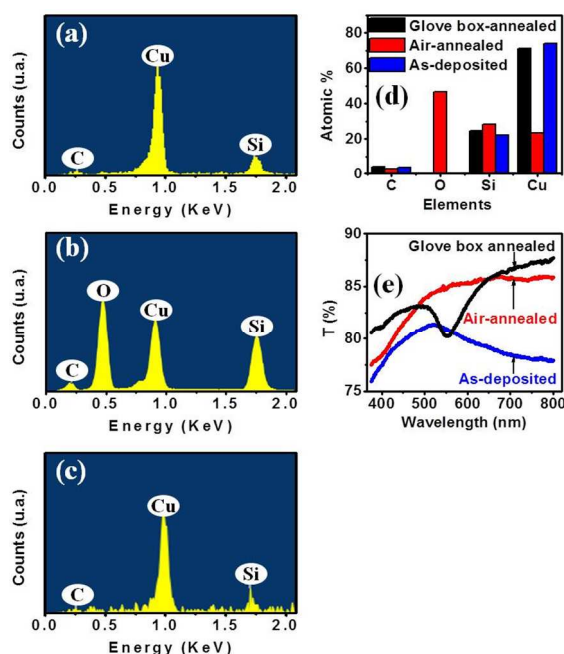


Fig. 2 EDX spectra showing the composition of Cu-NPs annealed at 300°C for 1 hr (a) in the glove box, (b) in air. (c) EDX of reference as-grown Cu-NPs. (d) Comparison of the elemental composition from Panels a, b and c. (e) Transmittance of Cu-NPs, as grown and annealed under different environmental conditions

The ratio of atomic content of O and Cu (Figure 2, panel d) shows that annealing in air lead to severe oxidation of the Cu-NPs, while the O level was below the detection threshold (< 1 at %) for the sample that was entirely annealed and treated inside

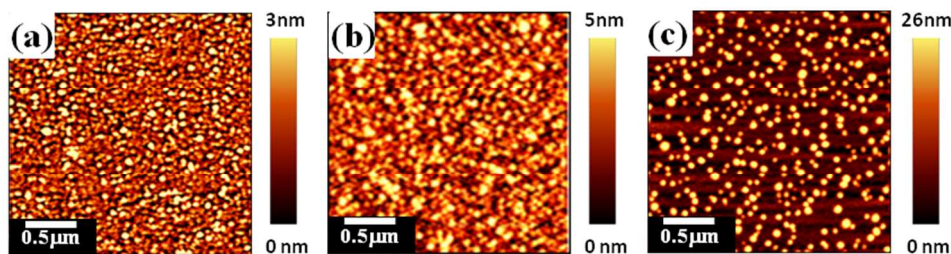


Fig. 3 AFM topography images of (a) as-deposited, (b) air-annealed and (c) glove box annealed Cu-NPs. Thermal annealing was at 300°C for 1 hour

In addition to thermal annealing of interconnected Cu-NPs, it was also possible to initiate further nucleation by island formation during sputtering, also known as Volmer-Weber growth²⁹ without any post-annealing process. In order to identify the optimal growth conditions for random arrays of Cu-NPs for plasmonic photovoltaic applications, we varied the Ar partial pressure in the chamber from 9 Pa to 23 Pa and sputtered a set of samples at -400 V dc negative bias voltage. External negative bias of the sample is essential to decrease the deposition rate and favor the process of nucleation during the sputtering deposition, thus promoting Volmer-Weber growth of individual Cu-NPs at

the glove box. Figure 2, panel e, shows the optical transmission spectra of these samples. A dip centered at $\lambda_p = 552 \pm 5$ nm, that can be assigned to resonant plasmon excitation^{25, 26}, is evident in the transmission spectrum, of the sample annealed and treated in glove box, while it is undetectable in the air-annealed sample as a result of surface oxidation²⁷. On the other hand, the transmittance of the reference as-deposited Cu-NPs shows a transmittance enhancement (i.e. a peak in transmittance)²⁸ at the opposite of plasmonic enhancement (i.e. a dip in transmittance, corresponding to a peak in reflectance). The transmittance enhancement corresponds to metallic behavior in this sample – the morphology of the Cu-NPs presented in the following paragraph shows that the nanoparticles are highly interconnected.

Figure 3 reports the atomic force microscope (AFM) images of the samples previously discussed in Figure 2. Panel (a) shows the morphology of the sample prior to annealing, with a fine distribution of interconnected Cu-NPs that gave rise to a transmittance peak in Figure 2e. Air annealing (Figure 3b) did not significantly alter the morphology of the sample. Although the Cu-NP diameter grows from 54 ± 5 nm to 61 ± 5 nm due to nucleation effects, particles are still interconnected and no plasmon-related feature was noticed in the optical transmission spectrum in Figure 2e due to significant oxidation. Conversely, more significant nucleation occurs upon annealing the sample in the glove box (Figure 3c), with well separated and oxygen-free nanoparticles of 73 ± 2 nm in diameter. This demonstrates that, by growing our samples in an UHV deposition system attached to a glove box, we are able to completely overcome the effects of oxidation and to produce random arrays of Cu-NPs of suitable quality for nanoplasmonics. More experimental evidence on the nucleation of these particles, including the scanning electron microscopy images and particles distributions under different experimental conditions, can be found in the Supplementary Information.

the opposite of interconnected particles²⁹. The average particle diameter increased from 58 ± 10 nm to 95 ± 10 nm with increasing chamber pressure. A complete characterization of this set of samples including AFM images, optical transmission spectra, collection-mode SNOM images and 3D-SNOM profiles of forward-scattered lights is reported in the Supplementary Information.

2.2 - 3D-SNOM Imaging

Figure 4 reports a typical example of one of our 3D-SNOM images obtained from the setup reported in Figure 1 and recorded

the random system of Cu-NPs growth at 12 Pa Ar pressure. The AFM image in panel (a) corresponds to the collection-mode SNOM image shown in panel (b), in which yellow pixels indicate regions from which larger intensity of light is forward-scattered and collected from the tip aperture and black pixel indicates no light being collected. From Figure 4b, it can be observed that at $z \approx 0$, in the proximity of the sample surface, the intensity of light forward-scattered by the bare glass substrate is significantly lower than the intensity of light scattered by the Cu-NPs. As can be observed from Figure 4a and 4b, the Cu-NP size cannot be considered to be much smaller than the illumination wavelength, λ . Therefore, when light interact with these particles, the scattered electric field is not purely dipolar in nature, but is formed by an infinite superposition of multipoles.⁶

According to Mie theory, the multipolar nature of the scattered field is expected to manifest itself with the fact that the field intensity undergoes a number of oscillations, with maxima and minima at specific distances z , from the surface of the particles.³⁰⁻³³ Experimentally, these oscillations are clearly visible in Figure 4c, that represent a (x, z) SNOM scan of the line at $y = \text{const.}$ indicated by letters A and A' in Figure 4b. No oscillations are visible if a bare glass substrate is scanned, which confirms that the forward-scattered near field that produces them must be attributed to the Cu-NPs. From Figure 4c, it can also be noticed that the light intensity is relatively uniform along the x -axis, with only relatively lower intensity in the correspondence of the largest particles. This is a consequence of the fact that even in this sample, in which the Cu-NPs are relatively sparse, the inter-particle distances are not significantly larger than a wavelength and, therefore, the Cu-NPs cannot be considered to be isolated. Figure 4d represents the integrated intensity of forward-scattered light along the A-A' cross section. Maxima corresponding to constructive interference and minima, corresponding to destructive interference, are clearly visible. It can be seen that for this specific sample, the first maximum of forward-scattered light intensity was observed at $\Delta z = 1200$ nm above the glass surface, while the absolute maximum occurs at about $\Delta z = 4400$ nm, after which the intensity of scattered light drops to very low values as can be expected from the poor green light transmittance of Cu-NPs in the far field.¹³

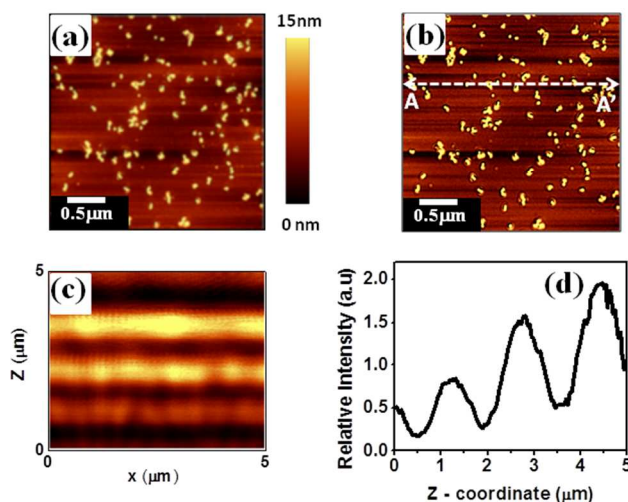


Fig. 4 (a) Topographic and (b) optical images obtained simultaneously from SNOM measurement on Cu-NPs sputtered at 12 Pa chamber

pressure. (c) Typical (x, z) SNOM intensity mapping performed along the A – A' cross section shown in Panel (b) and (d) the intensity profile showing the positions of constructive (maxima) and destructive (minima) interference of light scattered from Cu-NPs

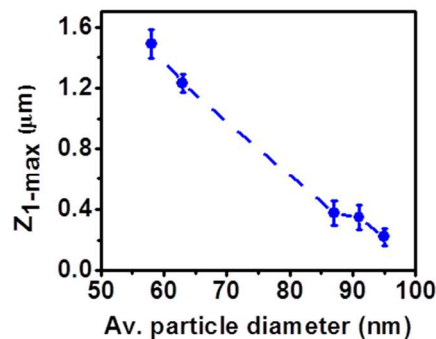


Fig. 5 Variation of scattered wave peak position with Cu-NPs diameters. Z_{1-max} represents the first significant peak intensity position of the scattered light obtained from (x, z) SNOM intensity profiles. The error bar corresponds to the standard deviation of 6 different intensity plots obtained from SNOM map

Using this very same procedure, we performed the 3D-SNOM scans on random arrays of Cu-NPs of different diameters, obtained from a set of samples deposited at increasing Ar pressures from 9 to 23 Pa (see the Supplementary Info for detailed characterization). In Figure 5 we show the variation of the first maximum of forward-scattered light intensity as a function of the average particle diameter and we observe that the light scattered from Cu-NPs with larger diameter is more closely coupled to the surface of the sample than in smaller Cu-NPs. For instance, Cu-NPs with 95 ± 10 nm diameter shows scattered wave peaks at $\Delta z_{1-\text{max}} = 220 \pm 50$ nm, compared to $\Delta z_{1-\text{max}} = 1400 \pm 100$ nm for the particles with 58 ± 10 nm diameter. This can be attributed to the dependence on the particle size of the cross-sections for optical absorption and scattering of light.⁵⁻⁷ The scattering cross-section is proportional to the square of the nanoparticle volume³⁴ and, subsequently, for sufficiently large nanoparticles it can be considered to be much greater than the cross-section for optical absorption. Therefore, for Cu-NPs with diameter greater than 80 nm, multipolar effects due to Mie scattering manifest themselves as strong coupling of the scattered waves in the vicinity of the NPs surface.

For any particle diameters, the values of $\Delta z_{1-\text{max}}$ measured by us are too large to use the radiation that is forward scattered by Cu-NPs in the near-field for harvesting light in organic thin film solar cells if the active layer is immediately overlaid in contact with the nanoparticle array. Typically, these devices are no thicker than 200 nm to minimize recombination of charges due to the high resistivity in the active layers.^{35,36} Decreasing the device thickness to a few hundred nanometers or less is also required to overcome recombination due to the short diffusion length of exciton generated within the active layer of the cell. As such, light absorption is generally limited by the thickness of the active layer. In order to use Cu-NPs for increasing organic solar cell performance, it is essential to position the active layer at a distance $\Delta z_{i-\text{max}}$ at which a maximum intensity of light is forward-scattered, for efficient concentration of light into the device. These considerations means that it would be beneficial to employ dielectric material for which the desired scattering effects are still

present but for which surface plasmon resonances do not occur.

We explored the prospect of this concept by developing a more structured plasmonic architecture in which a SiO₂ thin film, sputtered in the same chamber used to prepare our Cu-NPs, functions as spacer (see the Supplementary information for the detailed sputtering operation of the glass target). The AFM images, x-y SNOM images and 3D-SNOM images obtained with 100-nm diameter Cu-NPs with a 200 nm SiO₂ spacer and no spacer are reported in Figures 6a-c and 6d-f, respectively. On the one hand, from the AFM image in panel a, it can be observed that the surface of the sample is entirely flat after sputtering the SiO₂ spacer and the Cu-NPs are entirely embedded in SiO₂; on the other hand, the x-y transmission SNOM image in panel b clearly reveals the presence of Cu-NPs below the sample surface in that case. Conversely, in the absence of the spacer, Cu-NPs are visible at the very same locations in the AFM (panel d) and x-y transmission SNOM image (panel e) of Figure 6.

More interesting results arise from the comparison of the 3D-SNOM images with and without spacer, which are presented in panels c and f, respectively. In the presence of the spacer, we observe a broad region of constructive interference of forward-

scattered light, from zero to approximately 550 nm in the vicinity of the SiO₂ surface. This broad enhancement region may be assigned to coupling of plane waves normally incident to the SiO₂ surface with laterally propagating waves parallel to the SiO₂ surface, which result in the introduction of a lateral wave vector component.³⁷ Superposition of the lateral and normal components of the wave vector may also lead to increased intensity of the scattered light in addition to constructive interference in the normally incident wave. These results indicate that this architecture is extremely promising for building a near-field plasmon-enhanced solar cell on top of its surface. Conversely, in the absence of the spacer, a destructive interference peak is located at approximately 160 ± 30 nm from the sample surface, with results in considerable near-field depletion in the region at which the active layer of a solar cell would be placed in this case. Figure 7a shows the intensity profile of light scattered in the near-field along the z-axis, extracted from the 3D-SNOM images in Figures 6c and 6f. It can be observed that, in addition of a broader constructive interference peak, the structure with spacer produces a significantly higher intensity of forward-scattered light.

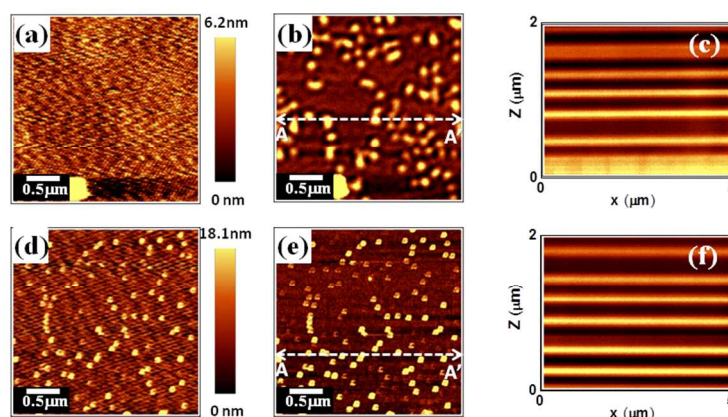


Fig. 6 (a) Topography, (b) corresponding optical image and (c) SNOM (x, z) intensity mapping along the A – A' cross section for Cu-NPs/SiO₂ spacer. The flatness of the topographic image is an indication that Cu-NPs are completely embedded in the 200nm SiO₂ spacer. Also shown is (d) topography, (e) corresponding optical image and (f) SNOM (x, z) intensity map for the reference bare Cu-NPs on glass substrate

2.3 - Solar cell fabrication and testing

In order to demonstrate the critical importance of our 3D-SNOM method for designing nanostructures for plasmonic enhancement, we have built and tested two identical bulk heterojunction (BHJ) organic solar cells on the top of our plasmonic architectures presented in Figures 7b and 7c, with and without a 200 nm SiO₂ spacer on top of Cu-NPs. Solar cell fabrication has been carried out in the glove box that was directly attached to the sputtering system used to fabricate the Cu-NPs and the SiO₂ spacer, without direct exposure of the sample to air. A 100 nm indium-tin oxide (ITO) thin film was spun directly on top of the two surfaces, with and without spacer, from a colloidal suspension of ITO in isopropanol. The as-spun samples were subsequently annealed at 400°C, a temperature that does not affect the morphology of Cu-NPs. This thermal treatment is essential for the colloidal ITO to coalesce and form a continuous ITO thin film of 150 Ω/sq sheet resistance. Anhydrous PEDOT:PSS in isopropanol was spun on the top of ITO to form a 30 nm hole transport layer. The solar cell active layer consisted in a 120-nm mixture of regioregular

Poly(3-hexylthiophene-2,5-diyl) (P3HT) and [6,6]-phenyl-C₆₁-butyric acid methyl ester (PCBM) spun from chlorobenzene.

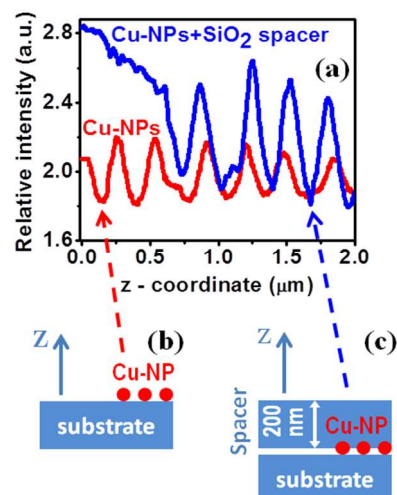


Fig. 7 (a) The intensity profiles showing the positions of the scattered wave enhancements from Cu-NPs/SiO₂ and the reference bare Cu-NPs measured by our (x, z) SNOM technique. Schematic diagram showing samples of Cu-NPs (b) without and (c) with 200 nm SiO₂ spacer light, with arrows pointing to the corresponding intensity profiles

Interdigitated bilayer metallic contacts of calcium (20 nm) and aluminum (100 nm) were fabricated in a thermal evaporator that was also installed in the same chamber housing the sputtering system, which resulted in four complete solar cells assembled on top of each one of our four plasmonic architectures. The schematic of these devices is shown in Figures 8a and 8b, respectively.

Device testing was also carried out in the glove box and produced the current-voltage (I-V) curves shown in Figures 8c and d, respectively. It can be observed that, although the dark characteristics of the two devices are basically the same, a significantly larger photocurrent could be extracted from the

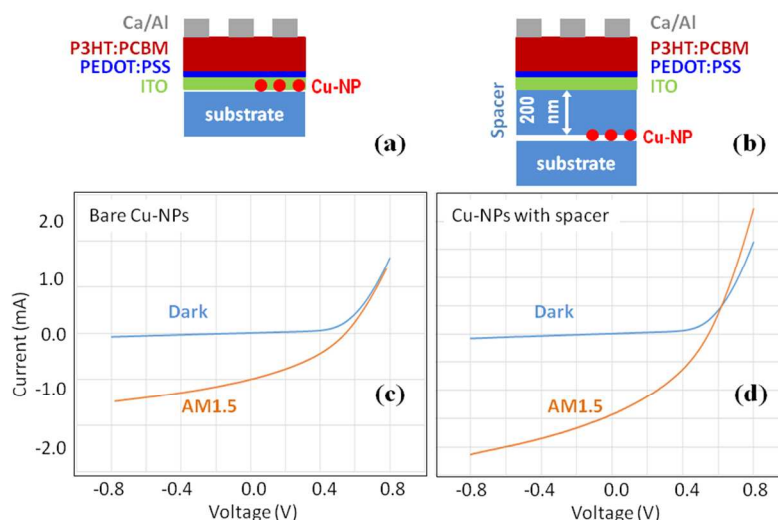


Fig. 8 The scheme of (a) the reference solar cell of bare Cu-NPs without a spacer and (b) the solar cell architecture designed with the aid of our 3D-SNOM results that includes a 200 nm SiO₂ spacer. I-V characteristics of the solar cells with Cu-NPs plasmonic layer (c) without and (d) with spacer between Cu-NPs and ITO-P3HT/PCBM organic active layer

3. Conclusion

Copper nanoparticles have been successfully deposited by radio frequency (RF) sputtering system for use as a plasmonic enhancement layer in thin film organic solar cells. Our deposition system, which comprises of coupled sputtering chamber, thermal evaporator and glove box was specifically set up to achieve the deposition of contaminant-free NPs from the high vacuum environment, while the storage and manipulation are carried out in inert atmosphere in the glove box. Cu-NPs of different diameters were obtained by varying the deposition chamber pressure and were used to study the scattering phenomenon arising from light interaction with the nanoparticles.

By introducing an innovative 3D scanning near-field optical microscope technique, we obtained the various positions of enhancement of plasmonic waves arising from multipolar contributions to scattering cross-section by Cu-NP ensembles. The best coupling of the scattered light to the sample surface was achieved by incorporating a 200 nm SiO₂ spacer between the Cu-

devices built on the architecture with spacer, which produced an average short-circuit current of $I_{sc} = 1.44$ mA, more than twice as the value ($I_{sc} = 0.67$ mA) obtained in the absence of the spacer. Conversely, the open circuit voltage ($V_{oc} \approx 0.56 \pm 0.02$ V) and fill factor ($52 \pm 2\%$) of the two types of devices did not undergo any noticeable differences. These results are a strong indication of the fact that the resulting increase in AM 1.5 photoconversion efficiency ($\eta = 3.08\%$ on average in the presence of the spacer vs. $\eta = 1.38\%$ in the absence of spacer) is a consequence of the enhancement of light conveyed within the active layer of the device due to near-field radiation forward-scattered by Cu-NPs. In order to further substantiate these findings an identical control cell was also fabricated without any underlying array of Cu-NPs and resulted in an efficiency ($\eta = 2.45\%$) that was intermediate between the two cases, which further corroborated the usefulness of our 3D-SNOM method for effectively identify specific conditions for plasmonic solar cell enhancement.

NPs and the sample surface. With this configuration, the scattered light waves extended up to 500 nm from the Cu-NP/SiO₂ surface. The observed improvement in the scattering enhancement from

Cu-NP/SiO₂ surfaces is ideal for improved performance in plasmonic devices such as thin film solar cells that are normally no more than 200 nm in thickness.

4. Experimental Details

The Cu-NPs we studied were deposited by Radio Frequency (RF) magnetron sputtering of a copper target with argon ions in a vacuum chamber. The deposition chamber is attached to nitrogen-filled glove box through a gate valve interconnect that allows for easy access to the chamber (see the Supplementary information for detailed description of our deposition system). Cu-NP of different sizes was deposited on microscope glass with RF power of 75 W for 3 minutes at increasing chamber pressures from 9 Pa to 23 Pa.

In order to verify the effect of oxidation on thermally treated Cu-NPs, we performed energy dispersive x-ray spectroscopy (EDX) analysis of the samples deposited at the same conditions but annealed at different environment using LEO (Zeiss) 1540 field emission scanning electron microscopy (SEM). This sample was sputtered on Si substrate for 3 minutes at 75W RF power, 0V dc bias voltage and 9 Pa Ar pressure and divided in two parts that were annealed separately at 300°C for 1 hour. The glove-box annealed sample was taken out immediately before being measured with a dwell time no more than 10 minutes before being admitted in the SEM/EDX chamber. UV-VIS transmittance of the NPs was measured at normal incidence in a range of wavelengths between 350 nm and 800 nm using a Varian DMS80 spectrophotometer. The transmittance data were obtained at a step scan of 10 nm per second.

Near field optical study and morphological mapping at the nanoscale were performed using a Witec Alpha 300S atomic force microscope. The Witec Alfa 300S, an aperture-type, AFM-integrated SNOM instrument can be used to record SNOM images and, simultaneously, AFM topographic images of a sample. The system can record SNOM images in 'transmission mode' or in 'collection mode' that differs in the way the sample is illuminated and the scattered light is collected. In the collection mode operation described schematically in Fig. 1a, light from a 532 nm green laser operated up to 50 mW (Excelsior, Spectra Physics Inc., serial no. 10398) is directed, by a system of optical fibers, into an inverted microscope, and the optical response of the sample is collected by the nanohole ($d \approx 80$ nm) located at the end of an AFM hollow tip, mounted below a high-resolution Confocal microscope. The collected light is subsequently launched via the confocal microscope into an optical fiber that is connected to a photomultiplier tube (U-68000, Hamamatsu) operating in photon-counting mode. The sample is positioned on a 100 x 100 μm piezo-scanner that has a maximum excursion of 10 μm in the z-direction. In addition, the mechanical arm on which the confocal microscope is mounted can also be moved in z-direction for optimizing the focal plane at the level of the AFM tip. If the hollow tip is sufficiently close to the sample surface, only the near-field optical response from the sample surface will be collected. However, if the hollow tip is lifted up at a controlled distance r from a nanoparticle that is located at the sample surface, all of the other normal modes representing the propagating component of the scattered waves can be detected.

In our SNOM collection mode operation, the sample surface is scanned along the (x, y) plane at $z = 0$, or in the (x, z) direction at $y = \text{constant}$, in order to obtain relevant information about the amount of light scattered by the particle at a distance $z = r$ from its surface, as demonstrated in Figure 1b. With this three-dimensional optical imaging procedure, specifically designed for this study, the collection mode SNOM analysis is carried out first to obtain the (x, y) nano-optical and topographic (contact-mode AFM) images of Cu-NPs, which are recorded simultaneously. We then choose a line at $y = \text{const.}$ from the (x, y) images and change the distance z from the tip to the sample surface. This can be done reproducibly because the piezo-scanner stage on which the sample is mounted allows us to control the sample – tip distance with ± 1 nm reproducibility.

The preparation of two identical organic solar cells with and

without a 200 nm SiO_2 spacer on top of Cu-NPs have been carried on following the same procedure reported elsewhere.³⁸

Both the fabrication and device testing has been performed in the glove-box, loaded with high-purity nitrogen, with oxygen and moisture levels less than 5 ppm. A 100 nm indium-tin oxide (ITO) thin film was spun directly on top of the two surfaces, with and without spacer, from a colloidal suspension of ITO in isopropanol. The samples were then fast-annealed at 400°C for 5 mins. Anhydrous Poly(3,4- Ethylene Di-Oxy-Thiophene):Poly-Styrene Sulfonate thin film (PEDOT:PSS, Aldrich cat. no. 483095) in isopropanol was spun at 3000 rpm on the top of ITO to form a 30 nm hole transport layer, and then baked on a hot plate at 140°C for 30 min. The solar cell active layers were assembled by spinning on the top of PEDOT:PSS a mixture (15 : 15 mg) of regioregular Poly(3-hexylthiophene-2,5-diyl) (P3HT) and [6,6]-phenyl-C₆₁-butyric acid methyl ester (PCBM) (Aldrich, cat no. 698989 and 684430, respectively) in chlorobenzene, followed by thermal annealing at 120°C for 15 min.

The solar cells were then transferred into the deposition chamber for thermal evaporation of Ca/Al bilayer backing electrodes. The metallic contacts (20 nm Ca thickness and 100 nm Al thickness, measured by a Sycom STM-2 thickness monitor) were evaporated on each solar cell using a patterned shadow mask³⁸, and resulting in a device area of 0.245 cm² each. The solar cell I–V characteristics were measured directly in the glove box using a Newport 9600 1.5 AM solar simulator at 1 sun. The solar simulator was calibrated using a Sciencetech SC-LT standard cell with certification accredited by the National Institute of Standards and Technology (ISO-17025).

Notes and references

- ^a Department of Physics and Astronomy, University of Western Ontario, London, Ontario N6A 3K7, Canada. E-mail: gfanchin@uwo.ca; Fax: +1-519-661-2033; Tel: +1-519-661-2111 ext. 86238
- ^b Department of Chemistry, University of Western Ontario, 1151 Richmond St., London, Ontario N6A 5B7, Canada
- [†]Electronic Supplementary Information (ESI) available: [Detailed description of the deposition system and a complete characterization of the set of samples deposited at different chamber pressures, including AFM images, optical transmission spectra, collection-mode SNOM images and 3D-SNOM profiles of forward-scattered lights are available in the Supplementary Information.]. See DOI: 10.1039/b000000x/
- [‡] Acknowledgements. This work is supported through the Natural Sciences and Engineering Research Council of Canada Discovery Grant program. GF acknowledges a Canada Research Chair in Carbon-based nanomaterials and financial support from the Canada Foundation for Innovation (CFI). HY acknowledges a MITACS Globalink summer award.
1. K. R. Catchpole, A. Polman, *Opt. Express*. **2008**, 16, 21793.
2. X. Gu, T. Qiu, W. Zhang, P.K. Chu, *Nanoscale Res. Lett.* **2011**, 6, 199.
3. E.E. Bedford, J. Spadavecchia, C. M. Pradier, F. X. Gu, *Macromol. Biosci.* **2012**, 12, 724.
4. D. Courjon, C. Bainier, *Rep. Prog. Phys.* **1994**, 57, 989.
5. M.A. Garcia, *J. Phys. D: Appl. Phys.* **2011**, 44, 283001.
6. C. F. Bohren, D. R. Huffman, *Absorption and Scattering of Light by Small Particles*, Wiley, New York, **1983**.
7. U. Kreibitz, M. Vollmer, *Optical Properties of Metal Clusters*, Springer Series in Material Science, **25**. Berlin: Springer, **1995**.
8. G. Mie, *Ann. Phys.* **1908**, 25, 377.
9. U. Kreibitz, B. Schmitz, H.D. Breuer, H. D. Breuer, *Phys. Rev. B*, **1987**, 36, 5027.
10. M. A. Garcia, S. Paje, J. Llopis, *Chem. Phys. Lett.* **1999**, 315, 313.
11. K.R. Catchpole, A. Polman, *Appl. Phys. Lett.* **2008**, 93, 191113.
12. Raether, Heinz, *Tracts in Modern Physics*, Springer **1980**, 88, 4.

13. H. Ehrenreich, H. Philipp, *Phys. Rev.* **1962**, 128, 1622.
14. S. Pillai, K. R. Catchpole, T. Trupke, M. A. Green, *J. Appl. Phys.* **2007**, 101, 093105.
15. S. Pillai, K. R. Catchpole, T. Trupke, G. Zhang, J. Zhao, M. A. Green, *Appl. Phys. Lett.* **2006**, 88, 161102
16. V.I. Belotelov, L.E. Kreilkamp, I.A. Akimov, A.N. Kalish, D.A. Bykov, S. Kasture, V.J. Yallapragada, Achanta Venu Gopal, A.M. Grishin, S.I. Khartsev, M. Nur-E-Alam, M. Vasiliev, L.L. Doskolovich, D.R. Yakovlev, K. Alameh, A.K. Zvezdin, M. Bayer, *Nature Communications.* **2013**, 4, 2128
17. Y. Song, W. Yin, Y. H. Wang, J. P. Zhang, Y. Wang, R. Wang, J. Han, W. Wang, S. V. Nair, H. E. Ruda, *Scientific Report.* **2014**, 4, 4991
18. Y. Song, Y. Wang, B.B. Li, C. Fernandes, H.E. Ruda, *Nanoscale.* **2013**, 5, 6779.
19. Y. Song, R. Li, Q. Sun, P. Jin, *Chem. Eng. Journal* **2011**, 168, 477.
20. I. Lisiecki, F. Billoudet, M.P. Pileni, *J. Phys. Chem.* **1996**, 100, 4160.
21. R.V. Kumar, Y. Mastai, Y. Diamant, A. Gedanken, *J. Mater. Chem.* **2001**, 11 1209.
22. S. Schiller, K. Goedicke, J. Reschke, *Surf. & Coating Technol.* **1993**, 61, 331.
23. L. Antonio, H. Steven, *Handbook of Photovoltaic Science and Engineering, 2nd Edition*, John Wiley & Sons, United Kingdom, **2011**.
24. B. Hecht, B. Sick, U. P. Wild, V. Deckert, R. Zenobi, O. J. F. Martin, D. W. Pohl, *J. Chem. Phys.* **2000**, 112(18), 7761
25. V. Halte, J. Y. Bigot, <http://www-ipcms.u-strasbg.fr/spip.php?rubrique311>.
26. E.D. Mozrzyk, P. Bieganski, *App. Optics*, **1993**, 32(13), 2345.
27. G.H. Chan, J. Zhao, E. M. Hicks, G.C. Schatz, R.P.V. Duyne, *Nano Lett.* **2007**, 7(7), 1947
28. N. Bonod, S. Enoch, L. Li, E. Popov, M. Neviere, *Optics Express.* **2003**, 11(5), 482
29. G. Cao, Y. Wang, *Nanostructures and Nanomaterials World Scientific*, **2011**, p.230 – 231.
30. B. Hecht, H. Bielefeldt, L. Novotny, Y. Inouye and D.W. Pohl, *Phys. Rev. Lett.* **1996**, 77(9), 1889
31. S.I. Bozhevolnyi, B. Vohnsen, I. Smolyaninov, A. V. Zayats, *Opt. Commun.* **1995**, 117, 417
32. D. Pohl, W. Denk, M. Lanz, *Appl. Phys. Lett.* **1984**, 44, 651.
33. O. Muskens, D. Christofilos, N. D. Fatti, F. Vallee, *J. Opt. A: Pure Appl. Opt.* **2006**, 8, S264
34. O. Stenzel, A. Stendal, K. Voigtsberger, C. V. Borczykowski, *Sol. Energy Mat. & Solar Cells*, **1995**, 37, 337.
35. W. Westphalen, U. Kreibig, J. Rostalski, H. Luth, D. Meissner, *Sol. Energy Mat. & Solar Cells*, **2000**, 61, 97.
36. E. T. Yu, D. Derkacs, S. H. Lim, P. Matheu, D. M. Schaadt, *Proc. of SPIE.* **2008**, 7033 70331.
37. H. R. Stuart and D. G. Hall, *Appl. Phys. Lett.* **1996**, 69(16), 2327.
38. R. Bauld, M. Hesari, M. S. Workentin, G. Fanchini, *Nanoscale*, **2014**, 6, 7570